4484 *Chem. Mater.* **2010,** *22,* 4484–4494
DOI:10.1021/cm101324n

CHEMISTRY OF MATERIALS
Article

Oxide Ion Conductivity, Phase Transitions, and Phase Separation in Fluorite-Based $Bi_{38-x}Mo_{7+x}O_{78+1.5x}$

Xiaojun Kuang,[†] Yuandi Li,[†] Chris D. Ling,[‡] Ray L. Withers,[§] and Ivana Radosavljević Evans*[,†]

[†]*Department of Chemistry, Durham University, Science Site, Durham DH1 3LE, United Kingdom,* [‡]*School of Chemistry, University of Sydney, Sydney, Australia, and* [§]*School of Chemistry, Australian National University, Canberra, Australia*

Received May 11, 2010. Revised Manuscript Received June 18, 2010

We present, for the first time, the ionic conductivity properties of two different, but closely related, bismuth molybdates: $Bi_{38}Mo_7O_{78}$ and $Bi_{37.5}Mo_{7.5}O_{78.75}$. Both are good oxide ion conductors, with the latter being comparable to yttria-stabilized zirconia. We show that the structure of $Bi_{38}Mo_7O_{78}$ is more complex than previously reported, and that this compound is a $5 \times 3 \times 6$ fluorite superstructure with slight monoclinic distortion. In addition to being a good oxide ion conductor, the material is noncentrosymmetric-polar and second harmonic generation (SHG) active. The second phase, orthorhombic $Bi_{37.5}Mo_{7.5}O_{78.75}$, reported for the first time, is an excellent oxide ion conductor. The materials have been characterized by impedance spectroscopy, variable-temperature synchrotron, neutron and laboratory powder X-ray diffraction, electron diffraction, and SHG measurements.

1. Introduction

Oxide-ion conductors are important functional materials with applications in oxygen sensors and pumps, as membranes for oxygen separation, and as electrolytes in solid oxide fuel cells. The cubic high-temperature form of bismuth oxide (δ-Bi_2O_3) is one of the best oxide-ion conductors known; however, it is stable only in a narrow temperature range (between 730 °C and 824 °C).[1] The underlying origin of ionic conductivity of δ-Bi_2O_3 is associated with its structural features: the simultaneous presence of a highly polarizable cation network and an intrinsically disordered oxygen-deficient anion sublattice. It has been shown that the structure of δ-Bi_2O_3 can be stabilized to room temperature via the partial substitution of Bi^{3+} by numerous cations, and this has led to the discovery of high oxide-ion conductivity in a large number of materials.[2]

Good oxide-ion conductivity has been found in $Bi_{26}Mo_{10}O_{69-\delta}$,[3] and more modest conductivities have been reported in several bismuth molybdates, including the Aurivillius-type Bi_2MoO_6 ($\sigma \approx 3 \times 10^{-4}$ S/cm at 650 °C) and the recently discovered family of compounds with a general formula $Bi_{2n+4}Mo_nO_{6(n+1)}$, $n = 3, 4, 5, 6$ ($\sigma \approx 1 \times 10^{-5}$–$1 \times 10^{-4}$ S/cm at 650 °C).[4−6] Further interest in bismuth molybdates stems from their catalytic activity for selective oxidation and ammoxidation of olefins[7,8] and the extraordinary structural complexity that some of them exhibit.[9]

Buttrey et al. first reported the compound $Bi_{38}Mo_7O_{78}$ in 1986,[10] and, based on electron diffraction studies, described it as an orthorhombic, oxygen-deficient, $5 \times 3 \times 3$ fluorite-type δ-Bi_2O_3 superlattice, with unit cell parameters of a = 28.658 Å, b = 16.818 Å and c = 16.903 Å, and space group *Pccn*. Interestingly, an early single-crystal X-ray diffraction (XRD) study reported a monoclinic unit-cell distortion for $Bi_{38}Mo_7O_{78}$, but this was interpreted as crystal twinning and not representative of the true unit cell of the material.[11] There was no further progress on the crystallographic characterization of this material until a recent structure determination from a single crystal of $Bi_{38}Mo_7O_{78}$ grown in an optical floating zone furnace.[12] The key finding in this work was that, contrary to the previous report, the true space group of $Bi_{38}Mo_7O_{78}$ is *Pbcn*. Using this space group, structure solution by direct methods gave a total of 24 metal sites (20 Bi and 4 Mo positions); the oxygen sublattice was completed by a combination of difference Fourier maps and *ab initio* modeling. This gave an ordered array of Bi and Mo cations, and an oxygen sublattice consisting of "fluorite-type" OBi_4 groups, with the remaining O atoms forming either tetrahedral or octahedral coordination environments around the

*Author to whom correspondence should be addressed. E-mail: ivana.radosavljevic@durham.ac.uk.

(1) Harwig, H. A. *Z. Anorg. Allg. Chem.* **1978**, *444*, 151.
(2) Shuk, P.; Wiemhofer, H. D.; Guth, U.; Gopel, W.; Greenblatt, M. *Solid State Ionics* **1996**, *89*, 179.
(3) Holmes, L.; Peng, L. M.; Heinmaa, I.; O'Dell, L. A.; Smith, M. E.; Vannier, R. N.; Grey, C. P. *Chem. Mater.* **2008**, *20*, 3638.
(4) Sim, L. T.; Lee, C. K.; West, A. R. *J. Mater. Chem.* **2002**, *12*, 17.
(5) Vila, E.; Rojo, J. M.; Iglesias, J. E.; Castro, A. *Chem. Mater.* **2004**, *16*, 1732.
(6) Vila, E.; Landa-Canovas, A. R.; Galy, J.; Iglesias, J. E.; Castro, A. *J. Solid State Chem.* **2007**, *180*, 661.
(7) Grasselli, R. K.; Burrington, J. D. *Adv. Catal.* **1981**, *30*, 133.
(8) Le, M. T.; Van Craenenbroeck, J.; Van Driessche, I.; Hoste, S. *Appl. Catal., A* **2003**, *249*, 355.
(9) Buttrey, D. J.; Vogt, T.; Yap, G. P. A.; Rheingold, A. L. *Mater. Res. Bull.* **1997**, *32*, 947.
(10) Buttrey, D. J.; Jefferson, D. A.; Thomas, J. M. *Mater. Res. Bull.* **1986**, *21*, 739.
(11) Ling, C. D. *J. Solid-State Chem.* **1999**, *148*, 380.
(12) Sharma, N.; Macquart, R. B.; Christensen, M.; Avdeev, M.; Chen, Y. S.; Ling, C. D. *J. Solid-State Chem.* **2009**, *182*, 1312.

 Published on Web 07/14/2010

Mo cations. The "fluorite-type" O atoms could be freely refined and gave sensible crystallographic parameters. Positions and isotropic temperature factors were refined for oxygens in MoO_4 groups; it was suggested that the somewhat-elevated temperature factors obtained ($b_{iso} \approx 4.7-15.8$ Å^2) could indicate rotational disorder of the MoO_4 tetrahedra, similar to that observed in $Bi_{26}Mo_{10}O_{69-\delta}$.[3] O atoms in the two crystallographically independent MoO_6 octahedra were less well-behaved. Therefore, their fractional coordinates were fixed at values obtained from density functional theory (DFT) modeling. An overall isotropic temperature factor was refined for each rigid MoO_6 octahedron, and the values obtained were quite high ($b_{iso} \approx 28.4$ and 44.2 Å^2); this was attributed to possible long-range disorder.[12]

In a recent structural study of oxide ion conductor lanthanum molybdate ($La_2Mo_2O_9$), which reported the crystal structure of the material at room temperature and its correlation with the high-temperature highly conducting structure, variable Mo coordination (4-, 5-, and 6-fold) was identified as a key feature providing the oxide ion migration pathway and thus facilitating fast ion conductivity in this material. The high-temperature cubic β-structure was described as a time average of the room temperature monoclinic α-$La_2Mo_2O_9$, and the onset of high oxide ion conductivity was associated with an order−disorder phase transition.[13] The key role of variable coordination on oxide ion mobility is also manifested in the recently identified interstitial oxide ion conductor melilite $La_{1+x}Sr_{1-x}Ga_3O_{7+0.5x}$, in which the mobile oxide interstitials are stabilized via formation of mixed GaO_4 and GaO_5 polyhedra in vertex-sharing tetrahedral layers.[14] The structural relationship between $Bi_{38}Mo_7O_{78}$ and δ-Bi_2O_3, the simultaneous presence of MoO_4 tetrahedra and MoO_6 octahedra in its structure and the high values obtained for oxygen atom displacement parameters suggesting disorder, prompted us to investigate further the properties of this material and its structural behavior.

In this paper, we report a detailed study of the Bi_2O_3−MoO_3 system around the Bi:Mo ratio of 38:7, focusing on the compositional, physical property, and structural aspects. We demonstrate that two different, but closely related, phases exist around this composition. Both exhibit oxide ion conducting properties and one is second harmonic generation (SHG) active.

2. Experimental Section

2.1. Synthesis. Polycrystalline samples were synthesized by solid-state reactions using Bi_2O_3 (Aldrich−Sigma, 99.9%) and MoO_3 (Alfa-Aesar, 99.95%) as starting materials. Initial syntheses were performed from a stoichiometric ($Bi_{38}Mo_7$) ratio of starting oxides, by heating the green mixture pellets in evacuated silica tubes at 840 °C for 72 h and slowly cooling back to room temperature. This method (with extended heating) was also used to produce a large (~8 g) sample on which both neutron and synchrotron XRD data were collected (*vide infra*). In later syntheses, the starting Bi:Mo ratio, the heating atmosphere, and the heating regime were varied. The starting materials were weighed either according to the stoichiometric cation ratio ($Bi_{38}Mo_7$) or an ~8.5% Mo excess ($Bi_{38}Mo_{7.6}$), mixed in agate mortar in isopropanol, and placed in alumina crucibles and covered with lids for calcination and firing. Mixtures were either fired directly at 840 °C, or first calcined at 600 and 700 °C (for 12 h at each temperature, with a heating and cooling rate of 5 °C/min and intermediate grindings after each calcination) and finally fired at 840 °C for additional 12 h. Syntheses under O_2 flow were also performed.

The pellets for electrical property characterization were made by uniaxially pressing the ground powder after the calcination at 600 and 700 °C, followed by sintering at 840 °C for 12 h, which led to pellets with ~80% theoretical density.

2.2. Variable-Temperature Powder X-ray and Neutron Diffraction. Variable-temperature X-ray diffraction (VT XRD) experiments on all materials were carried out on a Bruker Model AXS D8 Advance diffractometer with a Vantec detector, using Cu Kα radiation, equipped with an Anton Paar Model HTK1200 high-temperature attachment. Typically, the VT XRD data over a 2θ range of 5−90° were collected on heating and cooling between room temperature and 800 °C with a temperature increment of 40° and with a collection time of 2.3 h at each temperature. Room-temperature diffraction data to monitor phase content and low-temperature data were collected on a Bruker AXS D8 Advance diffractometer with a LynxEye detector, using Cu Kα radiation, equipped with an Oxford Cryosystems Model Phenix He closed-circuit cryostat. A thin layer of the finely ground sample was sieved onto a silicon slide and held in place by a small amount of petroleum jelly (Vaseline). The system was cooled from 300 K to 12 K at a rate of 15 K/h, and diffraction data were collected every 20 min in the 2θ range of 5°−90°.

Neutron diffraction data were collected at room temperature and 600 °C on a 6-g sample on instrument D2B at Institut Laue Langevin, using a Ge (335) monochromator (λ = 1.594 Å) and an array of 64 ^{3}He detectors spaced at 2.5° intervals. Nine scans in 25 steps of 0.05° at 75 s per step were recorded and summed, resulting in a total data collection time of 4.7 h at each temperature.

Synchrotron X-ray data collections on the same sample were performed at room temperature and 600 °C on the high-resolution powder diffraction beamline ID31 at the ESRF, using a wavelength of 0.3527 Å (determined from a Si standard). Polycrystalline sample was loaded into a 0.7-mm quartz capillary, which was rotated during data collection. Data were collected for 3 h at each temperature.

All powder diffraction data were analyzed using Topas Academic software.[15]

2.3. Electron Diffraction. Electron diffraction at room temperature was carried out in a Philips EM 430 transmission electron microscopy (TEM) system on crushed grains of the powder sample dispersed onto holey carbon-coated copper grids.

2.4. Impedance Spectroscopy. AC impedance spectroscopy measurements in air were carried out with a Solartron Model 1260 frequency response analyzer over a frequency range of $10^{-1}-10^6$ Hz. The pellets were coated with gold paste on each face and mounted in a ProboStat A-6 measurement cell and fired at 700 °C for 1 h to burn out the organic components in the paste to form gold electrodes. The impedance data were collected on heating and cooling between 60 and 700 °C. Zview3.0a software was used to analyze the complex impedance data.

(13) Evans, I. R.; Howard, J. A. K.; Evans, J. S. O. *Chem. Mater.* **2005**, *17*, 4074.
(14) Kuang, X.; Green, M. A.; Niu, H.; Zajdel, P.; Dickinson, C.; Claridge, J. B.; Jantsky, L.; Rosseinsky, M. J. *Nat. Mater.* **2008**, *7*, 498.
(15) Coelho, A. A. TOPAS-Academic, V4; Coehlo Software: Brisbane, Australia, 2005.

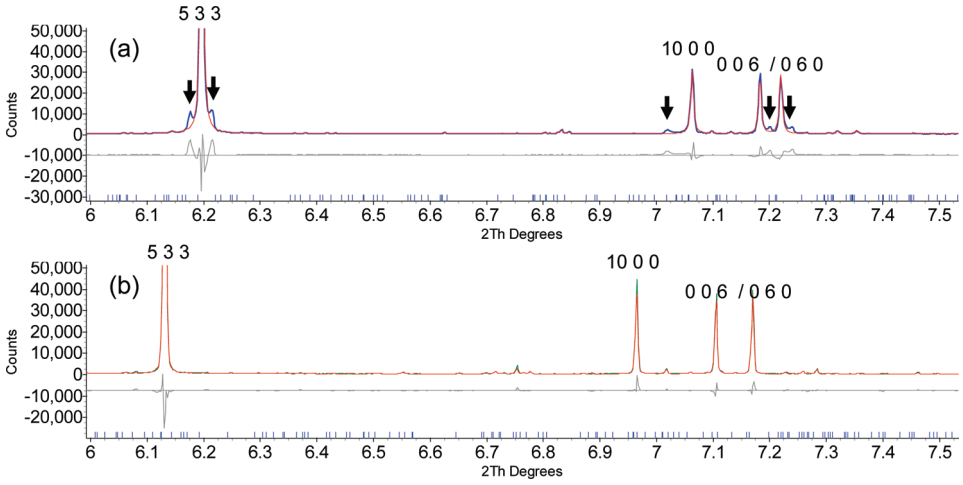

Figure 1. Rietveld fits to the synchrotron XRD data collected at (a) room temperature and (b) 600 °C, using the $Bi_{38}Mo_7O_{78}$ structural model in space group *Pbcn*. Extra peaks present in the room-temperature data, but not predicted by this orthorhombic unit cell, are marked with arrows.

2.5. ICP analysis. Approximately 20 mg of each sample analyzed was dissolved in dilute nitric acid (5 mL). The samples were subsequently diluted with 3% nitric acid prior to analysis (~Bi 170 ng/mL and Mo 15 ng/mL). Using inductively coupled plasma−mass spectroscopy (ICP-MS) (Perkin−Elmer Model Elan6000), optimized to reduce polyatomic interferences, calibration lines for Mo (mass 95 and 97) and Bi (mass 209) were generated from the serial dilution of 1000 ppm stock solutions (Romil). Two dilutions for each of the two samples were tested. Ten replicate measurements of each specimen were undertaken, with each replicate comprising of 25 sweeps of 50-ms dwell times per isotope, giving a total analysis time of ~40 s.

2.6. Complementary Measurements. Differential scanning calorimetry (DSC) was performed in air from ambient temperature to 200 °C, with a heating rate of 5 °C/min, on a Perkin−Elmer Model Pyris 1 instrument. SHG measurements were conducted using a modified Kurtz NLO system with a 1064-nm light source. The 532-nm SHG was collected in reflection and detected using a photomultiplier tube. A 532-nm narrow-bandpass interference filter was attached to the tube to only detect SHG light.[16]

3. Results and Discussion

3.1. Existence of an Orthorhombic Material and a Monoclinic Material. Initial attempts to use Rietveld fitting and the published structural model in space group *Pbcn*[12] to monitor the phase composition of our products showed weak reflections that could not be accounted for this orthorhombic unit cell. The extra peaks were particularly clear in the room-temperature synchrotron XRD pattern (marked with arrows in Figure 1a). Their intensities are up to 5% of the strongest Bragg peak (reflection 533, marked below, with an intensity of ~200 000 counts) in the diffraction pattern; however, they were absent from the dataset recorded at 600 °C (Figure 1b).

Attempts to account for these extra peaks by allowing a monoclinic distortion of the orthorhombic phase were not successful. Therefore, the *Pbcn* model was transformed to a triclinic structure in space group *P*1 and introduced as a second phase into the Rietveld refinement. All atomic coordinates were kept fixed, an overall isotropic temperature factor per phase and the cell parameters of the orthorhombic phase were refined, and several thousand cycles of simulated annealing were performed on the triclinic cell parameters of the second phase. In this process, two of the three freely varied angles refined to values of 89.99° and 90.01° (and were subsequently constrained to 90°), while the third showed a distortion to 90.5°, suggesting monoclinic metric symmetry for the second phase. The final unit-cell parameters obtained for the two forms were a = 28.65873(8) Å, b = 16.82208(5) Å, c = 16.90923(5) Å, and V = 8151.93(4) Å^3 for the orthorhombic phase, and a = 28.83526(35) Å, b = 16.77671(24) Å, c = 16.86861 (27) Å, α = 90.526(1)°, and V = 8160.0(2) Å^3 for the monoclinic phase. The final two-phase Rietveld fit obtained is shown in Figure 2; it shows that the investigated sample was a mixture of an orthorhombic material and a monoclinic material in a 92%:8% ratio.

The unexpected discovery of the monoclinic material, which was always present in our early syntheses, and the absence of any reference to it in the original paper describing the $Bi_{38}Mo_7O_{78}$ synthesis (which was carried out at 840 °C under flowing O_2),[10] prompted us to investigate the effects of different synthetic conditions on the product obtained more systematically. Details are summarized in Table 1.

Our results suggest that the phase composition of the final product is highly dependent on the initial green mixture composition and its thermal treatment. In our hands, the pure monoclinic material (M) forms when the stoichiometric (Bi:Mo = 38:7) green mixture is first precalcined at 600 and 700 °C and then fired at 840 °C for 12 h, either in a covered crucible or in O_2 flow (procedures 1 and 2 in Table 1; pattern 1 in Figure 3). Firing the stoichiometric green mixture directly at 840 °C, whether in alumina crucibles, evacuated silica tubes, or alumina boats under flowing O_2, gives monoclinic (M)/orthorhombic (O) mixtures with varying ratios of the two components where the M phase is the main phase at ~65−92 wt % (procedures 3−6 in Table 1; pattern 2 in Figure 3). However, repeated firing of the initial $Bi_{38}Mo_7$ composition at 840 °C in sealed evacuated silica tubes

(16) Ok, K. M.; Chi, E. O.; Halasyamani, P. S. *Chem. Soc. Rev.* **2006**, *35*, 710.

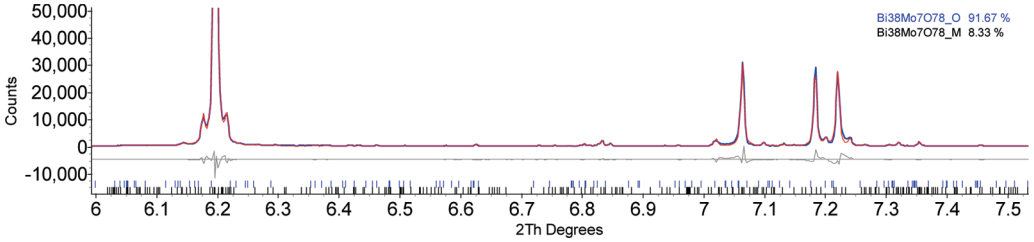

Figure 2. Two-phase Rietveld fit to the room-temperature synchrotron XRD data, showing a mixture of an orthorhombic phase and a monoclinic phase.

Table 1. Synthetic Procedures and the Phase Composition of the Products in Bismuth Molybdate Samples

procedure	initial composition[a]	thermal treatment/sample environment	final product
1	$Bi_{38}Mo_7$ (15.56%)	600 °C for 12 h 700 °C for 12 h 840 °C for 12 h Covered alumina crucible	Pure M phase
2	$Bi_{38}Mo_7$ (15.56%)	600 °C for 12 h 700 °C for 12 h 840 °C for 12 h Alumina boat under O_2 flow	Pure M phase
3	$Bi_{38}Mo_7$ (15.56%)	840 °C for 12 h Open crucible	Mixture O (25%)/M (75%)
4	$Bi_{38}Mo_7$ (15.56%)	840 °C for 12 h Covered alumina crucible	Mixture O (35%)/M (65%)
5	$Bi_{38}Mo_7$ (15.56%)	840 °C for 12 h Alumina boat under O_2 flow	Mixture O (8%)/M (92%)
6	$Bi_{38}Mo_7$ (15.56%)	840 °C for 72 h Sealed evacuated silica tube	Mixture O (30%)/M (70%)
7[b]	$Bi_{38}Mo_7$ (15.56%)	840 °C for 72 h 840 °C for 15 h Sealed evacuated silica tube	Mixture O (92%)/M (8%)
8	$Bi_{37.5}Mo_{7.5}$ (16.67%)	600 °C for 12 h 700 °C for 12 h 840 °C for 12 h Covered alumina crucible	Pure O phase
9	$Bi_{37.5}Mo_{7.5}$ (16.67%)	840 °C for 12 h Covered alumina crucible	Pure O phase

[a] Percentages given in brackets represent percent Mo_2O_6. [b] Samples made using procedure 6 were reground and refired for 15 h at 840 °C in a sealed evacuated silica tube.

with intermittent grinding (procedure 7 in Table 1) could change the mixture from the predominantly monoclinic to the predominantly orthorhombic material, as evidenced by quantitative analysis of the diffraction data. The pure orthorhombic material (O) forms when a Mo-rich green mixture is fired in a covered alumina crucible at 840 °C for 12 h, either with or without precalcination (procedures 8 and 9 in Table 1; pattern 3 in Figure 3).

3.2. Electron Diffraction. Having established reproducible synthetic routes to the two target materials, we used electron diffraction to confirm the unit cell and to determine the space group symmetry of the newly observed monoclinic phase. Electron diffraction patterns obtained for the two materials are shown in Figure 4. They show that the *c*-axis in the monoclinic phase is doubled, relative to the orthorhombic material, i.e., a 5 × 3 × 6 fluorite superstructure. The electron diffraction pattern in Figure 5 shows the spot twinning in monoclinic $Bi_{38}Mo_7O_{78}$,

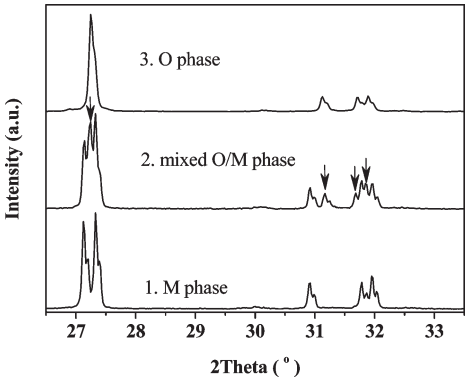

Figure 3. Laboratory XRD patterns of the orthorhombic phase (O), the monoclinic phase (M), and a mixed orthorhombic and monoclinic phase of bismuth molybdate. The reflections from the orthorhombic phase are marked with arrows in pattern 2.

from which the α angle can be estimated as being ~90.6°, in good agreement with the value of 90.526(1)°, obtained

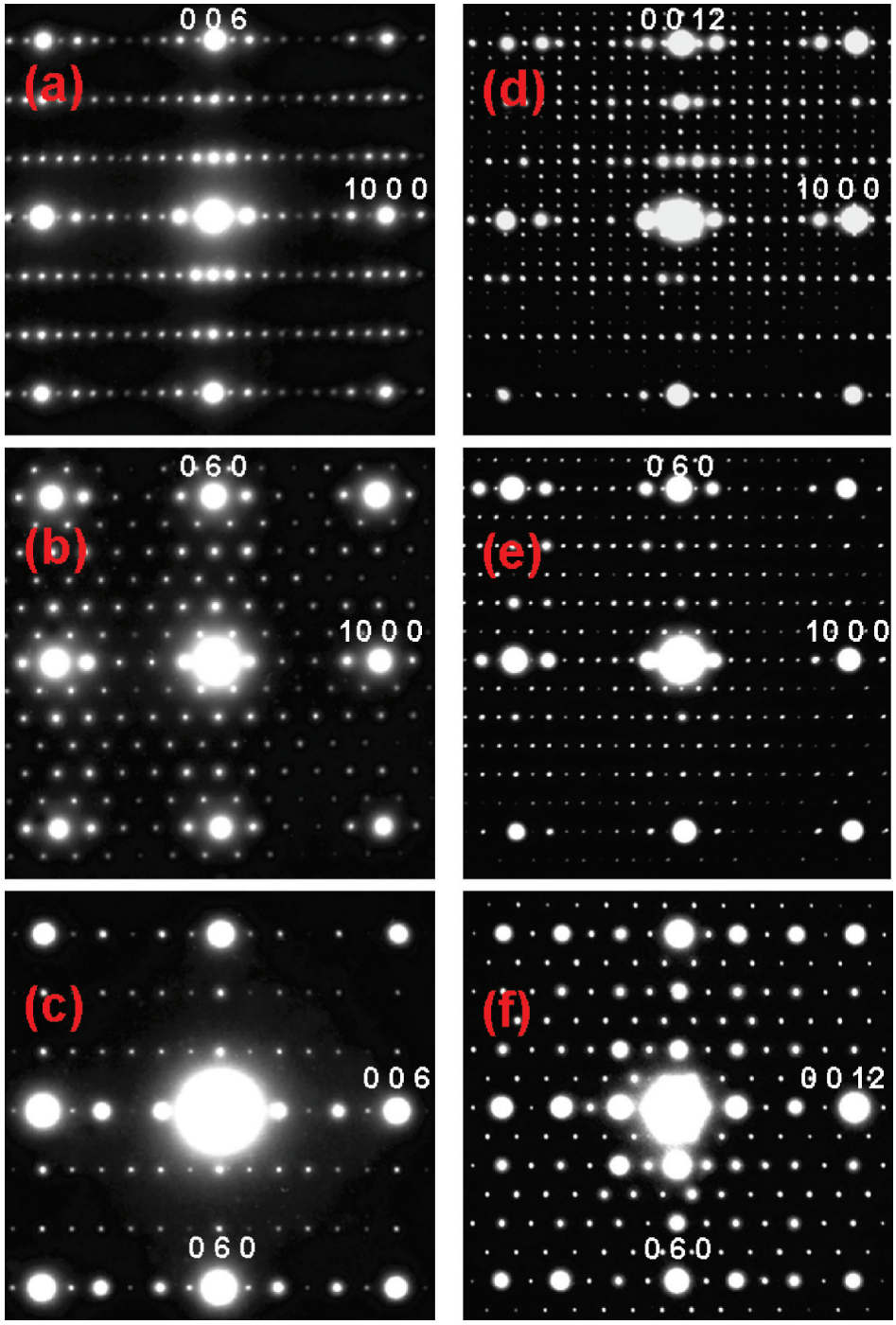

Figure 4. Electron diffraction patterns of (a−c) orthorhombic material ($5 \times 3 \times 3$ fluorite superstructure) and (d−f) monoclinic material with a doubled *c*-axis ($5 \times 3 \times 6$ fluorite superstructure).

from the unit-cell refinement against the ID31 synchrotron data.

Systematic absences in electron diffraction patterns suggest space group *Pn*11 or one of its centrosymmetric supergroups (*P*2/*n*11 or $P2_1/n11$). A positive SHG test, with an observed signal ~5 times greater than that of quartz, confirmed the noncentrosymmetric space group *Pn*11. In the large supercell observed by electron diffraction and this space group, the structure contains 152 unique Bi sites, 28 unique Mo sites, and 312 unique O sites, resulting in a total of 492 atoms in the asymmetric unit. Simulated annealing methods have previously been successfully applied simultaneously to XRD and neutron diffraction data to determine some of the most-complex structures solved from powder data, namely, the 136-atom ZrP_2O_7 and the 176-atom $Bi_2Sn_2O_7$.[17,18] However, the crystallographic complexity of the monoclinic $Bi_{38}Mo_7O_{78}$ with 492 unique atoms significantly surpasses these examples; in fact, it contains more unique atoms than the most-complex oxides (using this criterion) determined from

(17) Stinton, G. W.; Hampson, M. R.; Evans, J. S. O. *Inorg. Chem.* **2006**, *45*, 4352.
(18) Evans, I. R.; Howard, J. A. K.; Evans, J. S. O. *J. Mater. Chem.* **2003**, *13*, 2098.

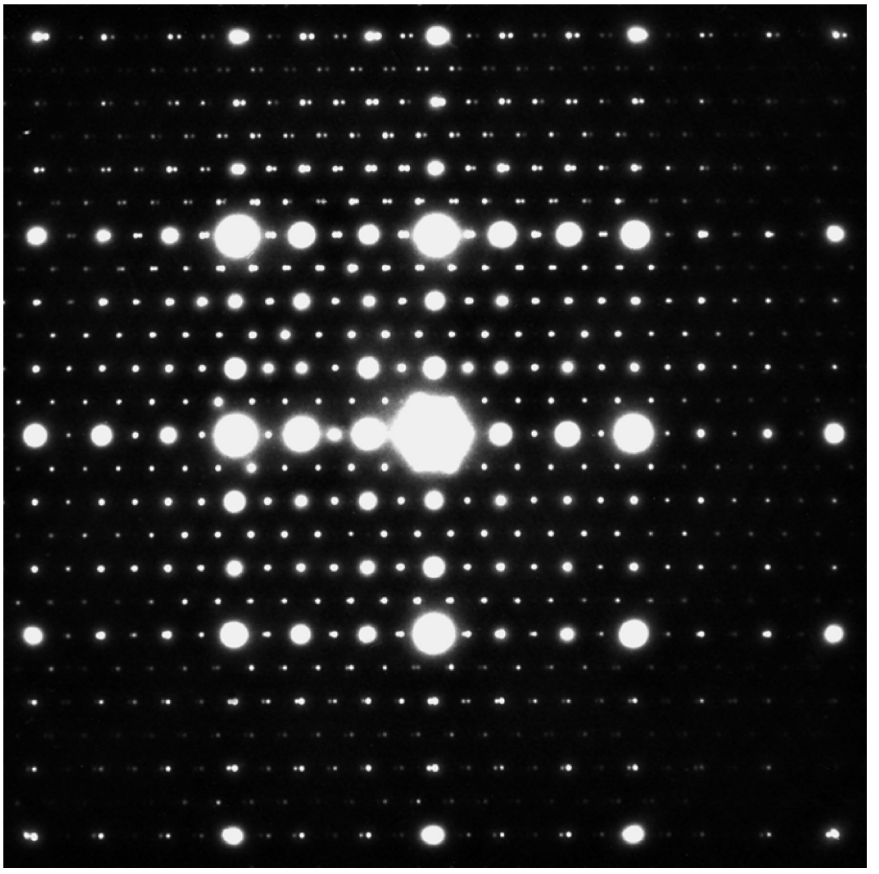

Figure 5. Electron diffraction pattern of monoclinic $Bi_{38}Mo_7O_{78}$ revealing the non-90° angle through spot twinning.

single-crystal diffraction data, reported in the literature (312-atom α-$La_2Mo_2O_9$, and the two polymorphs of $Mo_2P_4O_{15}$ with 253 and 441 unique atoms, respectively).[13,19,20]

3.3. Phase Transformations and Phase Separation. A comparison of our two synchrotron XRD datasets shows that the monoclinic phase present at room temperature disappears by 600 °C (Figure 1). To gain further insight into this transformation, we carried out differential scanning calorimetry (DSC) measurements and variable-temperature laboratory powder XRD. The differential scanning calorimetry (DSC) trace shown in Figure 6 suggests a phase transition that occurs gradually over a temperature range between 60 °C and 100 °C. In the same temperature region, we observe a gradual loss of intensity, followed by the disappearance of the Bragg peaks belonging to the monoclinic material, and their re-emergence on cooling (see Figure 7).

Complete and reversible conversion to an apparently single-phase orthorhombic material was observed reproducibly, whether the starting material was a pure monoclinic sample or an O/M mixture. This seems to suggest an apparent reversible temperature-dependent polymorphic transformation of $Bi_{38}Mo_7O_{78}$, occurring between 60 °C and 100 °C. The temperature of this transition and its sluggishness could potentially mean that a high-temperature O phase was getting quenched to room temperature in our early

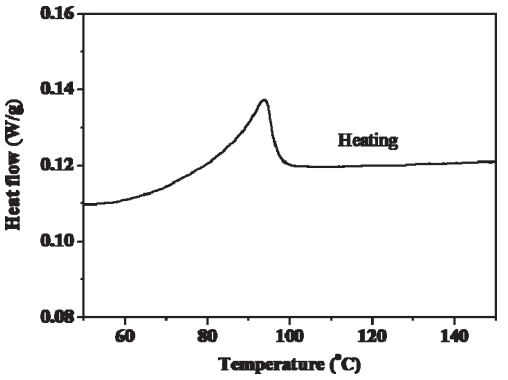

Figure 6. DSC curve of a mixed O/M phase bismuth molybdate sample.

synthetic attempts, which typically resulted in O/M mixtures. Therefore, we carried out numerous attempts to obtain a pure monoclinic material by annealing O/M mixtures just below the phase transition temperature and by cooling very slowly through the phase transition, but these attempts were not successful; such thermal treatments had no effect on the phase composition of the initial samples.

Several further variable-temperature powder XRD experiments were carried out on the bismuth molybdate samples to investigate their phase behavior and stability. To extract the dependence of the unit-cell parameters on temperature, data were analyzed by one or two-phase Rietveld fitting, as appropriate, using the structural model of Sharma et al.[12] for the orthorhombic phase and the transformed structure (with atomic coordinates fixed) for

(19) Lister, S. E.; Evans, I. R.; Howard, J. A. K.; Coelho, A.; Evans, J. S. O. *Chem. Commun.* **2004**, 2540.
(20) Lister, S. E.; Evans, I. R.; Evans, J. S. O. *Inorg. Chem.* **2009**, *48*, 9271.

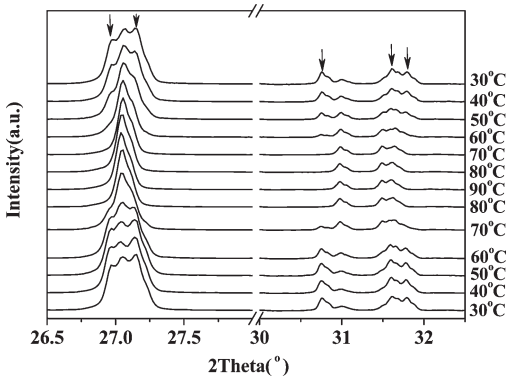

Figure 7. Variable-temperature powder XRD patterns of mixed orthorhombic and monoclinic bismuth molybdate sample. Arrows mark the reflections of the monoclinic phase.

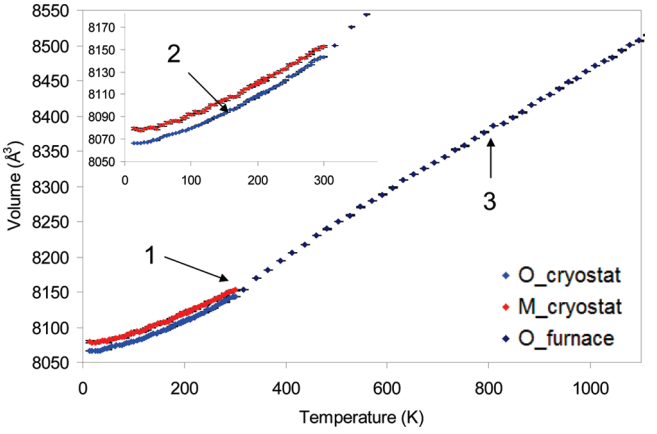

Figure 8. Temperature dependence of the unit-cell volumes of the orthorhombic and monoclinic bismuth molybdate phases.

the monoclinic phase. Figure 8 gives the plot of the unit-cell volumes obtained for the orthorhombic phase and the monoclinic phase in one such study performed between −258 °C (15 K) and 800 °C (1073 K), carried out on a sample which, as prepared, contained an O/M mixture (sample 7 in Table 1). Three important features should be noted on this plot: (1) the already discussed disappearance of the M phase above room temperature; (2) the persistence of both O and M phases on cooling to 15 K and an essentially constant unit cell volume difference of ~12 Å^3 (the M unit cell being larger); and (3) a small discontinuity in the O unit-cell volume at ~800 K.

The persistence of both materials to the lowest temperature observed, together with the inability to convert the O phase or the O/M mixtures into the monoclinic form by annealing and slow cooling, suggested that the orthorhombic and monoclinic materials were not simply polymorphs of $Bi_{38}Mo_7O_{78}$, but, in fact, had slightly different compositions, with the M phase being Bi-richer (as evidenced by its larger unit-cell volume, relative to the O phase; see Figure 8).

ICP analysis carried out on the pure O and M samples (made by synthetic procedures 8 and 1) confirmed this. Chemical analysis by ICP from 10 measurements on two specimens of the O and the M phase, consistently gave a

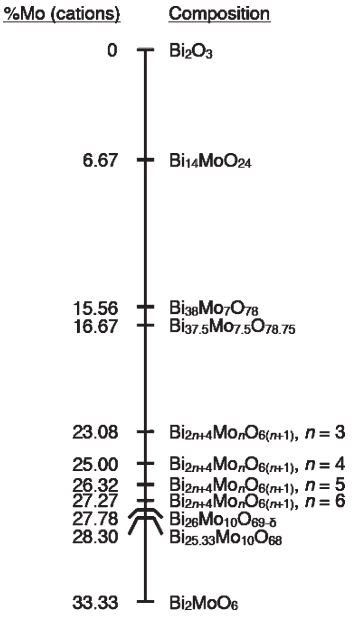

Figure 9. The Bi-rich end of the $Bi_2O_3-Mo_2O_6$ phase diagram.

higher Bi:Mo ratio for the latter, with average values of 5.5(1) for the monoclinic and 5.1(1) for the orthorhombic phase.

In light of these results, we propose that these two closely related materials are best described using the formula $Bi_{38-x}Mo_{7+x}O_{78+1.5x}$. The compositions that give the best agreements with the experimentally determined Bi:Mo ratios are the following: $x = 0$ for the M material ($Bi_{38}Mo_7O_{78}$, Bi:Mo = 5.4, 15.56% Mo_2O_6) and $x = 0.5$ for the O material ($Bi_{37.5}Mo_{7.5}O_{78.75}$, Bi:Mo = 5.0, 16.67% Mo_2O_6). Therefore, the Bi-rich end of the $Bi_2O_3-Mo_2O_6$ phase diagram should be modified. as shown in Figure 9.

3.4. High-Temperature Behavior of $Bi_{38-x}Mo_{7+x}O_{78+1.5x}$. As we have already shown from a variable-temperature experiment on a sample that initially contained both monoclinic $Bi_{38}Mo_7O_{78}$ and orthorhombic $Bi_{37.5}Mo_{7.5}O_{78.75}$, the former undergoes a phase transition to an orthorhombic structure gradually between 60 °C and 90 °C (see Figure 7). Results of a similar experiment conducted on the pure monoclinic $Bi_{38}Mo_7O_{78}$ sample, depicted in Figure 10, fully support this finding and also present two other interesting features: monoclinic and orthorhombic forms of this composition can coexist (e.g., at 80 °C on heating, 70 °C on cooling) and there is a hysteresis of ~10°, suggesting a first-order phase transition.

Beyond this phase transition, $Bi_{38}Mo_7O_{78}$ and $Bi_{37.5}Mo_{7.5}O_{78.75}$ become indistinguishable by powder diffraction, i.e., accidental peak overlap means that only one orthorhombic phase is observed. However, as pointed out earlier (see Figure 8), there seems to be a very subtle discontinuity in the unit-cell volume trend at ~800 K. This effect is observed more clearly in the temperature dependencies of the unit-cell parameters *a*, *b*, and *c*. Figure 11 shows the cell parameters for the same sample on which synchrotron and neutron diffraction data were collected, i.e., an O/M (92%/8%) mixture after it has transformed to apparently a single orthorhombic phase. The same effects are also observed when the

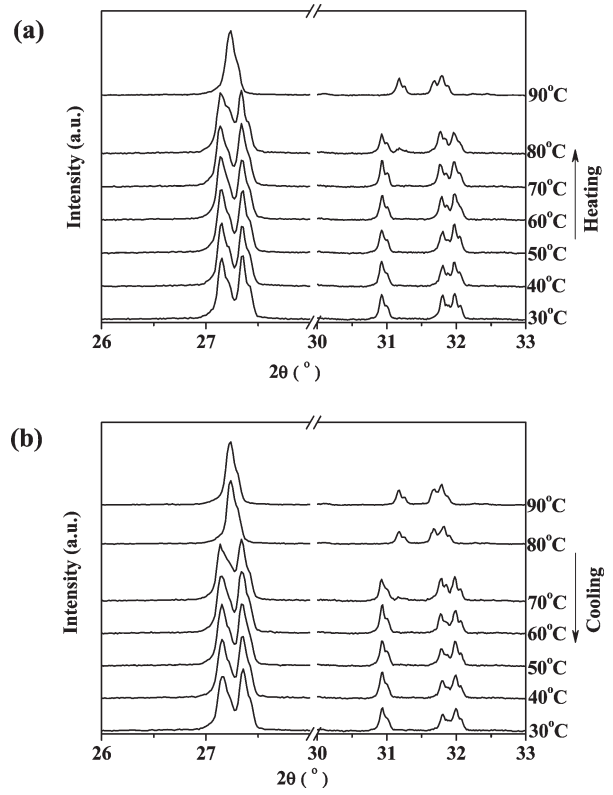

Figure 10. VT XRD data collected on the monoclinic $Bi_{38}Mo_7O_{78}$ upon (a) heating and (b) cooling from a variable-temperature run up to 150 °C, showing phase coexistence and a hysteresis.

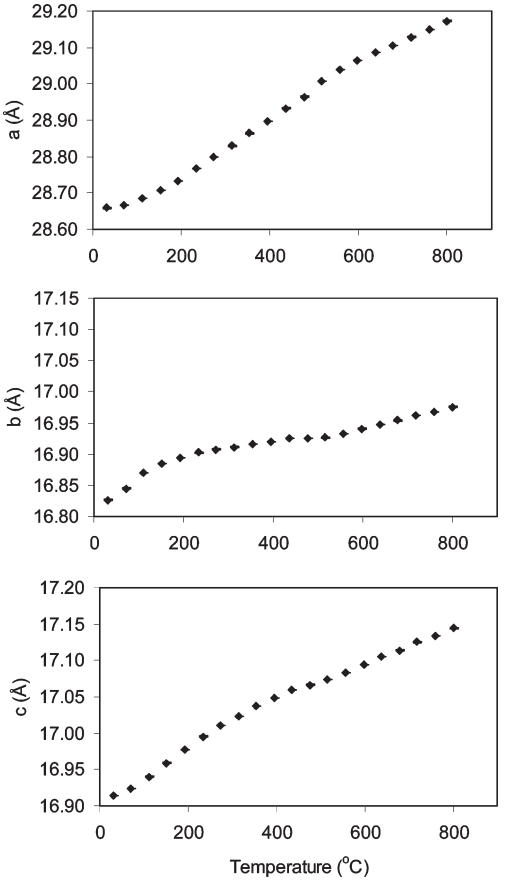

Figure 11. Temperature dependence of cell parameters of bismuth molybdate between room temperature and 800 °C.

same experiment is carried out on pure $Bi_{38}Mo_7O_{78}$ and pure $Bi_{37.5}Mo_{7.5}O_{78.75}$.

A careful comparison between our synchrotron XRD datasets collected at room temperature and 600 °C suggests that this phase transition may be associated with a disappearance of a number of extremely weak reflections. A low-angle subset of these is shown in Figure 12.

First, it should be emphasized that these reflections are very weak. In the ID31 data collected at room temperature, their intensities are ~0.5% of the strongest reflection in the pattern (533) and ~3% of the other fluorite sublattice reflections. However, they are fitted well by the existing structural model (Figure 12a). In the dataset collected at 600 °C, these reflections are absent (Figure 12b). A Rietveld fit of the published orthorhombic *Pbcn* $Bi_{38}Mo_7O_{78}$ structure to the combined ID31 synchrotron and D2B neutron diffraction 600 °C data with the atomic coordinates fixed and four isotropic temperature factors refined (one each for Bi, Mo, "fluorite" O atoms, and O atoms in MoO_n groups) gives the following agreement factors: R_{wp} (overall) = 7.66%, R_{wp} (X-ray) = 10.39%, R_{wp} (neutron) = 4.52%, R_{Bragg} (X-ray) = 6.00%, and R_{Bragg} (neutron) = 2.36%. The first three temperature factors refine to values expected for this temperature ($b_{iso} \approx 1.5-3.0$ Å^2), while the O atoms in MoO_n groups have very high temperature factors of $b_{iso} \approx 16$ Å^2. The main discrepancies are the nonzero intensities calculated for the weak peaks that have disappeared. When this structural model is allowed to relax slightly, a better fit to the data is achieved (see Figure 12c: R_{wp} (overall) = 5.56%, R_{wp} (X-ray) = 7.64%, R_{wp} (neutron) = 3.11%, R_{Bragg} (X-ray) = 3.54%, and R_{Bragg} (neutron) = 1.25%) and a narrower spread of both temperature factors and Mo bond valence sums is obtained. From the changes in the Mo−O bond lengths in MoO_n groups, it appears that these polyhedra distort and become less regular at high temperatures. However, a full structure refinement that would give insight into the nature and extent of possible O^{2-} disorder at high temperature requires neutron diffraction patterns of higher resolution than our current data or, ideally, single-crystal neutron diffraction data.

3.5. Ionic Conductivity in $Bi_{38}Mo_7O_{78}$ and $Bi_{37.5}Mo_{7.5}O_{78.75}$. AC impedance measurements were performed on pellets of monoclinic $Bi_{38}Mo_7O_{78}$ and orthorhombic $Bi_{37.5}Mo_{7.5}O_{78.75}$ upon heating and cooling. The phase compositions of pellets after the impedance measurement were examined by XRD and did not show any change, relative to the phase content prior to the measurement. The complex impedance data collected on the orthorhombic $Bi_{37.5}Mo_{7.5}O_{78.75}$ material comprised a single semicircular arc and a Warburg-type electrode response spike in the low-frequency range above 100 °C. Figure 13a shows a typical complex impedance plot of orthorhombic $Bi_{37.5}Mo_{7.5}O_{78.75}$ at 134 °C upon heating. The semicircular arc can be modeled with parallel resistor (R) and capacitor (C) elements. The capacitance associated with the bulk response estimated from $\omega RC = 1$ ($\omega = 2\pi f_{max}$, where f_{max} is the frequency at maximum imaginary impedance Z''_{max}, the intercept of the semicircular arc at low frequency was extracted as the bulk resistivity R_b) is ~6.4 pF/cm, which is close to the value of

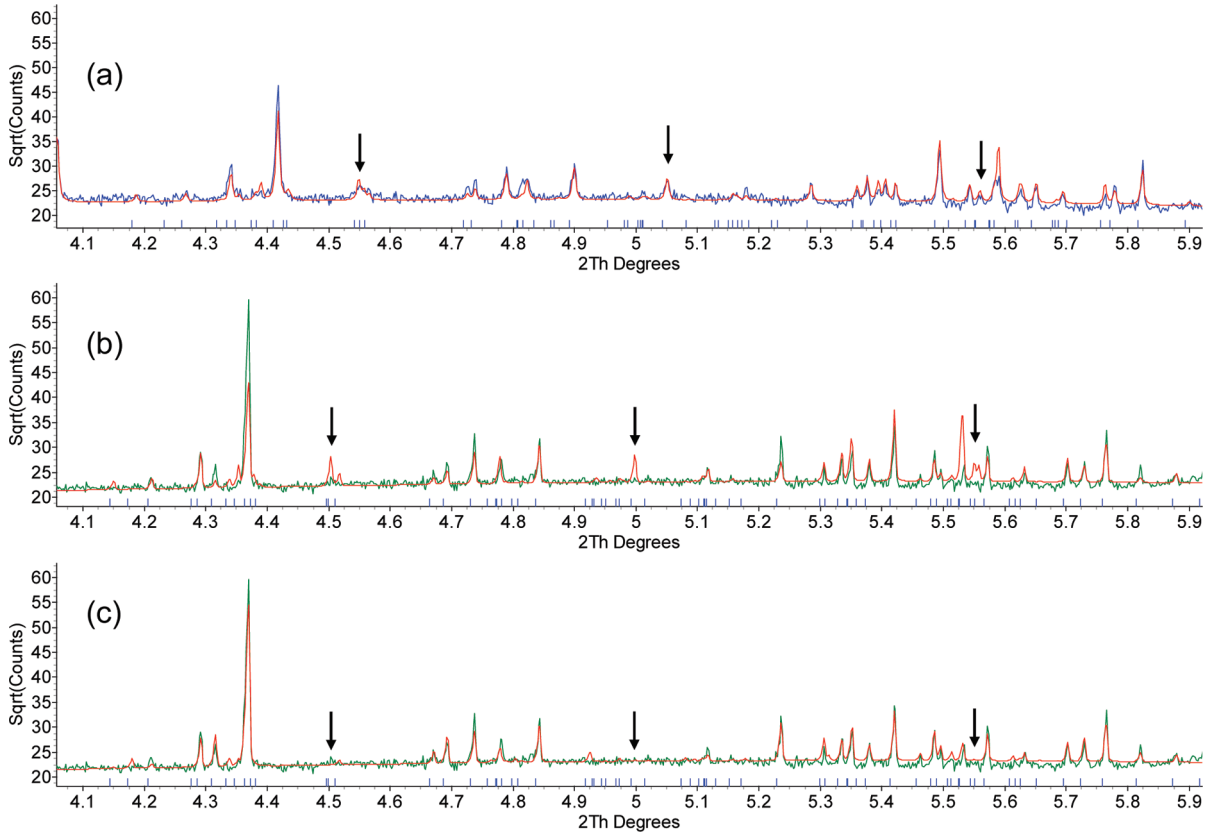

Figure 12. Subtle changes observed in the synchrotron XRD are marked with arrows: (a) weak peaks present at room temperature and calculated by the orthorhombic *Pbcn* structural model; (b) peaks have disappeared by 600 °C; and (c) a small relaxation of the structural model leads to zero intensities for these peaks, in agreement with the pattern observed at 600 °C.

5.8 pF/cm, estimated from the maximum imaginary modulus M''_{max}, using the equation $\varepsilon_0/(2M''_{max})$[21] ($\varepsilon_0$ is the capacitance of free space; $\varepsilon_0 = 8.854 \times 10^{-14}$ F/cm). This indicated that the Z'' peak is associated with the same *RC* elements as the modulus peak and the semicircular arc can be ascribed to a single bulk response.[22,23] The intercept of the semicircular arc was extracted as the bulk resistivity R_b, which can be treated as the total conductivity here, because no significant grain-boundary response was detected in the impedance data. The electrode response showed large capacitance within $10^{-8}-10^{-5}$ pF from 10 Hz to 0.1 Hz above 200 °C, which suggests an ionic conduction response.[22] With increasing temperature, the grain responses gradually disappeared and the electrode response dominated the impedance data, which gradually collapsed down to a semicircular arc (Figure 13b). The intercept at the high-frequency end of this arc was extracted as the bulk resistivity at high temperature. For the monoclinic $Bi_{38}Mo_7O_{78}$ pellet above 100 °C, apart from the electrode response, the impedance data contained a semicircular arc (Figure 13c), comprising two components of grain and grain-boundary responses, which led to two capacitance plateaus and electrical modulus peaks (inset in Figure 13c) for grains and grain boundaries, respectively. The intercept of the semicircular arc at low frequency was extracted as the total resistivity for monoclinic $Bi_{38}Mo_7O_{78}$. The noticeable contribution from grain boundary to the total resistivity in the monoclinic $Bi_{38}Mo_7O_{78}$ made the total conductivity for the monoclinic $Bi_{38}Mo_7O_{78}$ about an order of magnitude lower than that for the orthorhombic $Bi_{37.5}Mo_{7.5}O_{78.75}$ over the measured temperature range (see Figure 14a).

The Arrhenius plots of the total conductivity of the two materials upon heating and cooling are shown in Figure 14a, which show curvature for both materials, coinciding with the temperatures at which the temperature dependence of all cell parameters showed slight changes in slope (Figure 11). The activation energies at the high-temperature region (400−700 °C) are 0.774(8) and 0.81(2) eV for orthorhombic $Bi_{37.5}Mo_{7.5}O_{78.75}$ and monoclinic $Bi_{38}Mo_7O_{78}$, respectively. The Arrhenius plots of bulk conductivity of pure orthorhombic $Bi_{37.5}Mo_{7.5}O_{78.75}$ upon heating and cooling is essentially identical. Slightly higher conductivity on cooling than that on heating was observed for the monoclinic $Bi_{38}Mo_7O_{78}$, which could perhaps be ascribed to a small amount of the orthorhombic phase forming at elevated temperatures (although below the detection limit via laboratory XRD). Such a composition shift toward a lower Bi/Mo ratio on prolonged heating was observed in our synthetic experiments (and is described in section 3.1). Figure 14b shows the total conductivity of the orthorhombic $Bi_{37.5}Mo_{7.5}O_{78.75}$ within a temperature range of 350−700 °C, in comparison with the conventional $Zr_{0.92}Y_{0.08}O_{1.96}$ (YSZ),[24] $Bi_{0.8}Er_{0.2}O_{1.5}$ (EDB),[24] $Bi_{26}Mo_{10}O_{26}$,[25] and the most-conducting

(21) Morrison, F. D.; Sinclair, D. C.; West, A. R. *J. Am. Ceram. Soc.* **2001**, *84*, 531.
(22) Irvine, J. T. S.; Sinclair, D. C.; West, A. R. *Adv. Mater.* **1990**, *2*, 132.
(23) Leon-Reina, L.; Losilla, E. R.; Martinez-Lara, M.; Martin-Sedeno, M. C.; Bruque, S.; Nunez, P.; Sheptyakov, D. V.; Aranda, M. A. G. *Chem. Mater.* **2005**, *17*, 596.

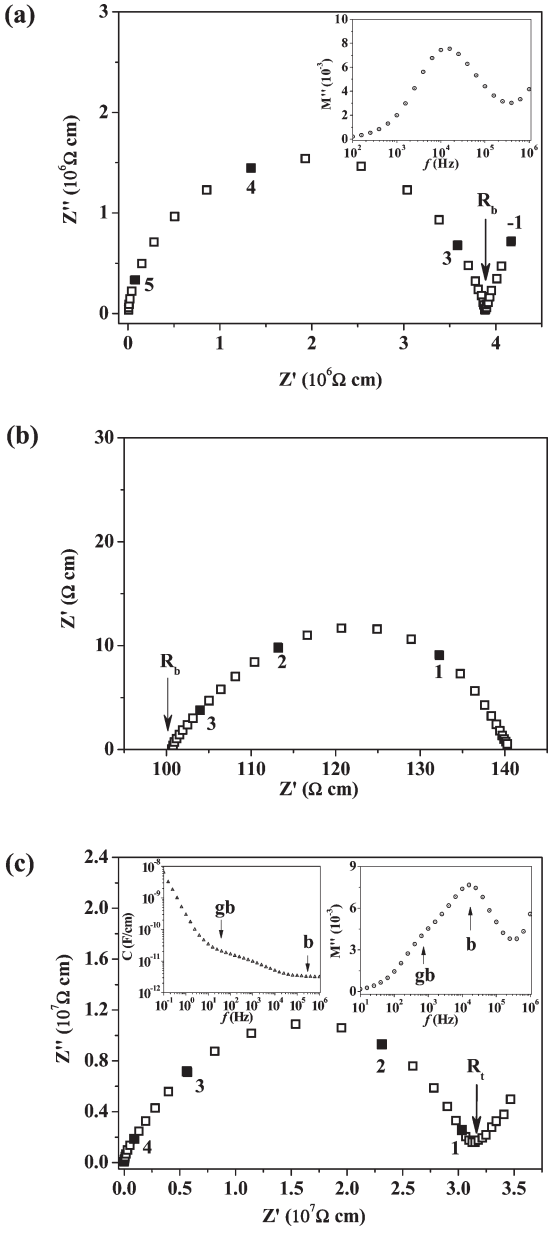

Figure 13. Complex impedance $Z''-Z'$ plots of pure orthorhombic phase $Bi_{37.5}Mo_{7.5}O_{78.75}$ pellet at (a) 134 °C and (b) 709 °C and (c) pure monoclinic phase $Bi_{38}Mo_7O_{78}$ pellet at 107 °C. The inset in panel (a) shows the frequency dependency of the imaginary modulus M''. The insets in panel (c) show the capacitance (C) and M'', as functions of the frequency. The numbers denote the selected frequency logarithms at the points marked by filled squares in each plot. The symbols "gb" and "b" denote grain boundary and bulk, respectively. R_b and R_t denote the bulk resistivity and total resistivity, respectively.

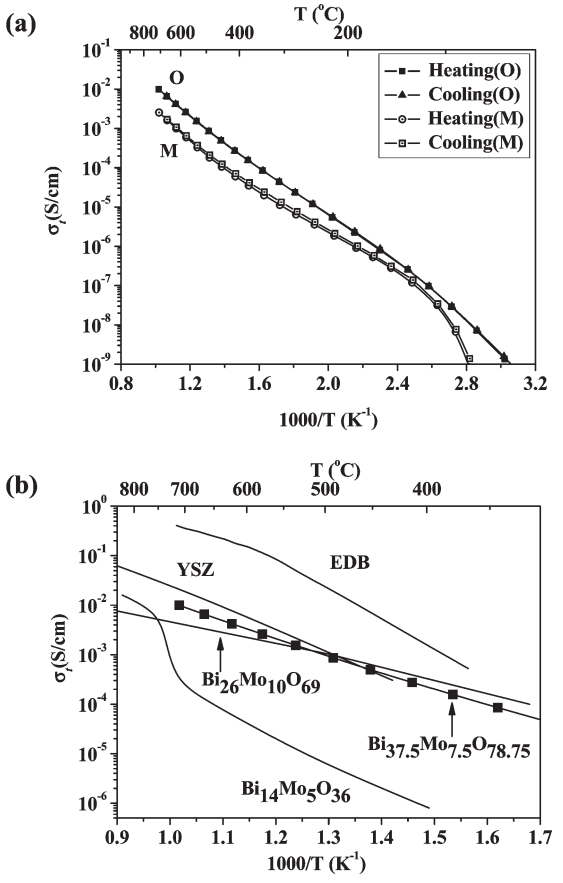

Figure 14. (a) Arrhenius plot of total conductivity of orthorhombic $Bi_{37.5}Mo_{7.5}O_{78.75}$ (O) and monoclinic $Bi_{38}Mo_7O_{78}$ (M) pellets upon heating and cooling. (b) Comparison between the total conductivities of $Bi_{37.5}Mo_{7.5}O_{78.75}$, conventional $Zr_{0.92}Y_{0.08}O_{1.96}$ (YSZ),[24] $Bi_{0.8}Er_{0.2}O_{1.5}$ (EDB),[24] $Bi_{26}Mo_{10}O_{69}$,[25] and the most conducting $Bi_{14}Mo_5O_{36}$[6] member in the fluorite-related $Bi_{2n+4}Mo_nO_{6(n+1)}$ system.

$Bi_{14}Mo_5O_{36}$ member of the fluorite-related $Bi_{2n+4}Mo_nO_{6(n+1)}$ system.[5,6] From 500 °C to 700 °C, $Bi_{37.5}Mo_{7.5}O_{78.75}$ shows a total conductivity of $10^{-3}-10^{-2}$ S/cm, which is slightly lower than that of YSZ, comparable to that of $Bi_{26}Mo_{10}O_{69}$, and better than the recently reported fluorite-related bismuth molybdates ($Bi_{2n+4}Mo_nO_{6(n+1)}$). The conductivities of $Bi_{37.5}Mo_{7.5}O_{78.75}$ and $Bi_{38}Mo_7O_{78}$ agree well with those reported by Takahashi et al.[26] for ~12−18 mol % Mo-doped Bi_2O_3 materials, which showed that the oxygen transport number was >0.95 for the materials with 14−33 mol % Mo within 500−800 °C. Therefore, the conduction can be predominantly ascribed to the oxide ion, which presumably also applies to the bismuth molybdates (15−17 mol % Mo) in this study.

4. Conclusions

Two closely related phases with a general formula $Bi_{38-x}Mo_{7+x}O_{78+1.5x}$ exist in the $Bi_2O_3-MoO_3$ phase system around the Bi:Mo ratio of 38/7. The $Bi_{38}Mo_7O_{78}$ ($x = 0$) material, which was previously thought to be an orthorhombic 5 × 3 × 3 fluorite derivative, is shown to be a more-complex 5 × 3 × 6 superstructure with a slight monoclinic distortion. At ~90 °C, it undergoes a reversible phase transition to an orthorhombic structure. The material is noncentrosymmetric (space group *Pn*) and second harmonic generation (SHG)-active. The $Bi_{37.5}Mo_{7.5}O_{78.75}$ ($x = 0.5$) composition is an orthorhombic 5 × 3 × 3 fluorite superstructure, crystallizing in space group *Pbcn*. Both materials are fast ion conductors, with the orthorhombic $Bi_{37.5}Mo_{7.5}O_{78.75}$ material displaying conductivity comparable to that of yttria-stabilized zirconia (YSZ).

(24) Kharton, V. V.; Marques, F. M. B.; Atkinson, A. *Solid-State Ionics* **2004**, *174*, 135.
(25) Vannier, R. N.; Mairesse, G.; Abraham, F.; Nowogrocki, G. *J. Solid-State Chem.* **1996**, *122*, 394.
(26) Takahashi, T.; Esaka, T.; Iwahara, H. *J. Appl. Electrochem.* **1977**, *7*, 31.

Acknowledgment. I.R.E. and X.K. thank the EPSRC for funding (through Grant No. EP/F030371). C.D.L. received support from the Australian Research Council−Discovery Projects (No. DP0666465). Irena Margiolaki (ESRF), Emmanuelle Suard (ILL), Sarah Lister, and John Evans (Durham University) are acknowledged for their assistance with synchrotron X-ray and neutron data collections. We also thank Douglas Carswell (Durham University) for thermal analysis and Jeongho Yeon and Shiv Halasyamani (University of Houston) for the SHG measurements.